
Path-independent Flow Matching for Multi-parameter Generative Dynamics

Francisco Téllez*
Université de Montréal, Mila

AmirHossein Zamani*
Concordia University, Mila

Philippe Martin*
Université de Montréal, Mila

Shuang Ni
Université de Montréal, Mila

Guy Wolf
Université de Montréal, Mila

Eugene Belilovsky
Concordia University, Mila

Sina Sanjari[†]
Royal Military College of Canada

Yanlei Zhang[†]
Queen’s University, Mila

Abstract

Flow Matching is a powerful framework for learning transport maps between probability distributions. Yet its standard single-parameter formulation is not designed to capture multi-parameter variations where the resulting transport should be path-independent. Path independence is crucial because it ensures that transformations depend only on the initial and target distributions, not on the specific path. In this work, we introduce *Path-independent Flow Matching (PiFM)*, a method for learning vector fields whose induced flows yield path-independent transport between distributions. We show that PiFM generalizes Flow Matching to higher-dimensional parameter domains while enforcing structural conditions that ensure consistency of composed transformations. In addition, we show that, under suitable assumptions, PiFM approximates the Wasserstein barycenter, linking the framework to a notion of distributional interpolation. To enable practical training, we propose a tractable, simulation-free objective that regresses onto multi-parameter conditional probability paths. We showcase empirically that PiFM outperforms other approaches on both synthetic and real world data in interpolating path-independent trajectories and generating desired out of distribution samples.

1 Introduction

Learning transformations between probability distributions is a central problem in modern machine learning, with applications spanning generative modeling, domain adaptation, trajectory inference, and scientific discovery. In these settings, one seeks not only to match target distributions, but also to understand how distributions relate through structured, continuous transformations such as the flows of vector fields. Recent neural approaches achieve this by reducing population-level objectives to sample-wise computations, enabling scalable training via stochastic optimization. This paradigm underlies VAEs (Kingma & Welling, 2022; Diederik & Max, 2019), GANs (Goodfellow et al., 2014; S & Durgadevi, 2021), diffusion models (Ho et al., 2020; Song et al., 2021), and continuous-time transport methods (Chen et al., 2019; Grathwohl et al., 2018; Lipman et al., 2023; Tong et al., 2023, 2024), and has led to growing interest in modeling distributions through dynamical systems.

A broad class of methods, including continuous normalizing flows (Chen et al., 2019; Grathwohl et al., 2018), diffusion and score-based models (Ho et al., 2020; Song et al., 2021; Koehler et al., 2022; Berner et al., 2022), and Schrödinger bridges (Léonard, 2013; Bortoli et al., 2023; Liu et al., 2023), can be interpreted as learning time-varying transport dynamics that push a source distribution toward

*Equal contribution

[†]Co-senior authors

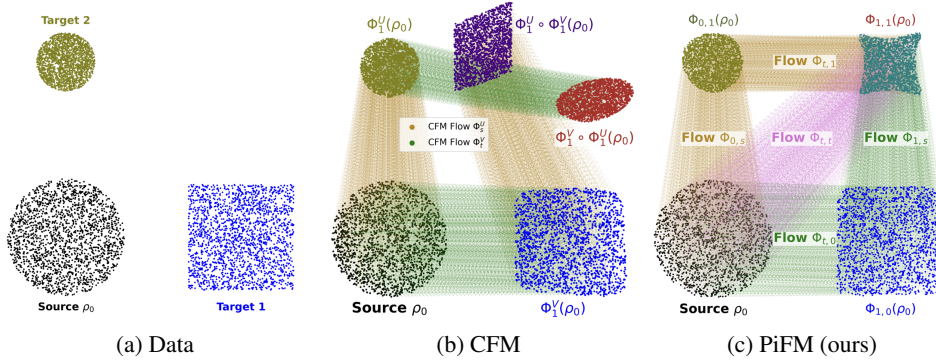


Figure 1: Learned trajectories for multi-marginal transport between a source (unit disc) and two targets (square, small disc). Traditional CFMs do not commute by composing flows of two separate processes, whereas PiFM (ours) is able to model commutative multi-process trajectories.

a target. Among these, Flow Matching (Lipman et al., 2023; Liu, 2022) provides a particularly simple and simulation-free training principle by directly regressing neural vector fields toward reference conditional velocities induced by a prescribed probability path. Conditional Flow Matching (Tong et al., 2023, 2024) and related extensions further generalize this idea, unifying several continuous-time generative frameworks by allowing transport between a broader family of source and target distributions.

Despite their success, existing flow matching methods are inherently limited to a single time parameter, implicitly assuming that all variations can be ordered along a single temporal axis. In many real-world settings, however, data are influenced by multiple independent processes that evolve concurrently and should compose in a path-independent manner. This arises naturally in settings such as biological perturbations acting on time-evolving cellular populations in single-cell genomics (Lotfollahi et al., 2023; Jiang et al., 2025), compositional attributes like shape and color in images (Wang et al., 2024), and modular transformations in physical systems (Neary & Topcu, 2023). Naively composing independently trained flows generally leads to non-commutative dynamics, where the final distribution depends on the order of application, limiting interpretability and downstream geometric reasoning as tasks such as analogy completion or attribute extrapolation become ill-defined when transformations fail to commute.

To address this limitation, we introduce *Path-independent Flow Matching (PiFM)*, a framework for learning multi-parameter generative dynamics driven by vector fields with path-independent transport of distributions. PiFM models probability paths over multiple temporal domains and enforces path independence through structural conditions on the vector fields, echoing classical commutativity and integrability criteria for flows (Lee, 2003; Warner, 1983; Ralph Abraham & Ratiu, 1984). This yields a well-defined notion of composing transformations, enabling consistent interpolation, extrapolation, and analogy-like operations in distribution space. We further establish a connection between PiFM and Wasserstein barycenters (Agueh & Carlier, 2011; Bigot & Klein, 2017), interpreting PiFM as a natural generalization of multi-marginal generative modeling (Cao et al., 2019; Albergo & et al., 2023; Beier et al., 2022; Pass, 2015), extending beyond the simplex structured parameter space in the Wasserstein Barycenter setting. Lastly, we evaluate PiFM through several computational experiments ranging from image translation and adaptive target generation to synthetic datasets for demonstration purposes.

Our contributions are summarized as follows:

1. **Path-independent Flow Matching (PiFM):** We introduce PiFM, a multi-parameter Flow Matching framework driven by vector fields. We establish the existence of path-independent flows and derive the sufficient integrability conditions ensuring consistency.
2. **Conditional-to-Marginal Flow Consistency:** We show how conditional probability paths induce coherent marginal dynamics in the multi-parameter setting. This leads to a training objective that combines vector field regression with a path-independence regularizer, which we further show becomes unnecessary in the affine case.
3. **Connection to Wasserstein Barycenters:** We establish a connection between PiFM and Wasserstein barycenters, enabling both interpolation and extrapolation of distributions.

4. **Empirical Validation:** We demonstrate the effectiveness of PiFM on synthetic and image translation tasks. PiFM outperforms prior methods such as Meta Flow Matching (Atanackovic et al., 2025) and Curly Flow Matching (Petrović et al., 2025) in low-dimensional domain shift settings, and achieves improved compositionality and consistency in high-dimensional multi-attribute image translation. We further validate PiFM on a dense single-cell reprogramming dataset (Schiebinger et al., 2019), treating experimental day and pluripotency score as two interacting flows to test path-independent generation in a high-dimensional, multi-stage biological process.

The paper is organized as follows. Section 2 reviews the necessary background on flow matching. Section 3 introduces the PiFM framework, its theoretical properties, and its connection to Wasserstein barycenters. Section 4 presents experimental results in both low-dimensional synthetic domain-shift settings and high-dimensional image translation tasks and single-cell application.

2 Background: Flow Matching and Minibatch Optimal Transport

The primary objective in distribution matching is to recover a transport map $\psi : \mathbb{R}^d \rightarrow \mathbb{R}^d$ for some $d \geq 1$ that transports a source density $q(a)$ to a target density $q(b)$. This push-forward requirement, denoted $q(b) = [\psi]_{\#}(q(a))$, underpins both optimal transport and modern generative modeling. In the empirical setting, where we lack analytical access to densities and observe only finite datasets $\{x_0^i\}_{i=1}^N \sim q(a)$ and $\{x_1^j\}_{j=1}^M \sim q(b)$, the challenge lies in approximating ψ from discrete samples. A powerful approach to model ψ is through dynamical systems, specifically ordinary differential equations (ODEs), which motivate the Flow Matching approach.

Flow Matching (Liu, 2022; Lipman et al., 2023; Tong et al., 2023; Albergo & Vanden-Eijnden, 2023) provides a framework for learning a dynamical system by establishing a correspondence between a probability density path $p : [0, 1] \times \mathbb{R}^d \rightarrow \mathbb{R}_{\geq 0}$ and a vector field $v : [0, 1] \times \mathbb{R}^d \rightarrow \mathbb{R}^d$. We say that p_t is generated by v_t if the pair (v, p) satisfies the following *continuity equation*

$$\frac{\partial p_t(x)}{\partial t} + \nabla \cdot (p_t(x)v_t(x)) = 0, \quad (1)$$

subject to the boundary condition $p_0 = q(a)$ and $p_1 = q(b)$.

While solving for the marginal vector field directly is intractable, *Conditional Flow Matching* (CFM) circumvents this by exploiting the linearity of (1) and considering the marginal densities $p_t(x)$ as a mixture of a simpler conditional densities $p_t(x|z)$ conditioned on a latent variable z (which might be a specific source-target data pair). In the CFM setting, the conditional densities $p_t(x|z)$ are induced by a conditional vector field $u_t(x|z)$. Consider a latent variable z with a density q . Then, $p_t(x) = \int p_t(x|z)q(z) dz$, and by defining the unconditional vector field $u_t(x)$ by $u_t(x) := \mathbb{E}_{q(z)} \left[\frac{u_t(x|z)p_t(x|z)}{p_t(x)} \right]$, (Lipman et al., 2023) showed that when the conditional vector field $u_t(x|z)$ generates the conditional probability path $p_t(x|z)$, the unconditional vector field $u_t(x)$ generates the marginal probability path $p_t(x)$.

For CFM, a vector field $v^\theta(t, x)$ is trained to approximate the intractable unconditional vector field by regressing onto the conditional fields. The CFM learning objective is to find θ that minimizes the loss function $\mathcal{L}_{\text{CFM}}(\theta)$ given by

$$\mathcal{L}_{\text{CFM}}(\theta) = \int \mathbb{E}_{z \sim q, x \sim p_t(\cdot|z)} \left[\|v_\theta(t, x) - u_t(x|z)\|^2 \right] dt.$$

This formulation enables simulation-free training of continuous normalizing flows by sampling $t \sim \mathcal{U}(0, 1)$, $z \sim q(z)$, and $x \sim p_t(\cdot|z)$, relying on efficient sampling from $q(z)$.

The density $q(z)$ can be specified in different ways. In independent CFM (I-CFM), $q(z) = q(a)q(b)$, while in optimal transport CFM (OT-CFM), $q(z) = \pi(a, b)$, where π is an optimal transport coupling between $q(a)$ and $q(b)$. Training under I-CFM uses independently sampled pairs (a, b) , whereas OT-CFM requires sampling from π , typically approximated via mini-batch optimal transport due to the cubic time and quadratic memory cost of full OT (Cuturi, 2013). Despite being approximate, mini-batch OT preserves the transport geometry in expectation and performs well empirically (Fatraş et al., 2021); the exact OT-CFM objective is recovered when the batch size equals the full dataset.

3 Multi-parameter Flow Matching and Path Independence

We begin by introducing a multi-parameter flow matching formulation. To simplify our notations, we restrict our exposition to the case of two independent parameters, denoted by t and s (see Section

A.1 for details on the more general case). Then, we introduce the PiFM framework, which extends CFM to a multi-parameter setting. We present the modeling choices and assumptions that form the foundation of PiFM, and show how these elements collectively ensure coherent marginal generation and path-independent transport of distributions. Finally, we describe how to train PiFM using a deep learning approach and establish a connection to the Wasserstein Barycenter. Proofs are included in the Appendix A.2 and Appendix A.3.

3.1 Multi-parameter Flows and Path Independence

Suppose we have two continuously differentiable vector fields $u, v : [0, 1]^2 \times \mathbb{R}^d \rightarrow \mathbb{R}^d$ depending on parameters t and s with associated ODEs:

$$\frac{\partial \phi}{\partial t}(t, s) = u_{t,s}(\phi(t, s)), \quad \forall s \in [0, 1] ; \quad \frac{\partial \psi}{\partial s}(t, s) = v_{t,s}(\psi(t, s)), \quad \forall t \in [0, 1]. \quad (2)$$

With initial conditions $\phi_{0,0}(x) = x$ and $\psi_{0,0}(x) = x$, both equations are well-defined at $(t, s) = (0, 0)$, yielding the functions $\phi_{t,0}$ and $\psi_{0,s}$. These solutions can then be used to define consistent initial conditions along the axes, namely $\phi_{0,s}(x) = \psi_{0,s}(x)$ and $\psi_{t,0}(x) = \phi_{t,0}(x)$, which in turn determine the full solutions $\phi_{t,s}$ and $\psi_{t,s}$. Note that this construction proceeds by solving ODEs sequentially, existence and uniqueness at each stage are guaranteed by standard ODE theory (see, e.g., (Wiggins, 2003)). Associated with these solutions, we define the flow maps $\Phi, \Psi : [0, 1]^2 \times \mathbb{R}^d \rightarrow \mathbb{R}^d$ by $\Phi_{t,s}(x) = \phi_{t,s}(x)$ and $\Psi_{t,s}(x) = \psi_{t,s}(x)$.

Analogous to the one-parameter setting, the vector fields $u_{t,s}$ and $v_{t,s}$ generate densities $p_{t,s}$ and $q_{t,s}$, respectively, provided that the following continuity equations hold for all $t, s \in [0, 1]$:

$$\frac{\partial p_{t,s}(x)}{\partial t} + \nabla \cdot (p_{t,s}(x) u_{t,s}(x)) = 0 \quad \frac{\partial q_{t,s}(x)}{\partial s} + \nabla \cdot (q_{t,s}(x) v_{t,s}(x)) = 0. \quad (3)$$

Similarly to the definition of initial conditions for ODEs, we prescribe boundary conditions along the coordinate axes. Given an initial density ρ_1 and target densities ρ_2 and ρ_3 , we define the boundary conditions by setting $p_{0,s} = (\Psi_{0,s})\#\rho_1$, $p_{1,s} = (\Psi_{1,s})\#\rho_2$, $q_{t,0} = (\Phi_{t,0})\#\rho_1$ and $q_{t,1} = (\Phi_{t,1})\#\rho_3$. With these constructions, the continuity equations yield consistent transport of $p_{t,s}$ along the flow $\Phi_{t,s}$ and of $q_{t,s}$ along the flow $\Psi_{t,s}$.

We say the transport flow is distributionally path-independent (or commutative) if

$$(\Phi_{t,s})\# \circ (\Psi_{0,s})\# p_{0,0} = (\Psi_{t,s})\# \circ (\Phi_{t,0})\# p_{0,0}, \quad \forall t, s \in [0, 1]. \quad (4)$$

Intuitively, (4) states that moving first along the t -direction while fixing $s = 0$ using the flow $\Phi_{t,s}$, and then along the s -direction using $\Psi_{t,s}$, yields the same result as performing the operations in the reverse order. The implication this has for path independence is that if we consider a parametrized path $\gamma(l) : [0, 1] \rightarrow [0, 1]^2$, with $\gamma(l) = (\gamma^{(1)}(l), \gamma^{(2)}(l)) = (t(l), s(l))$, then (4) implies that the order in which we apply the transport maps $\Phi_{\#}$ and $\Psi_{\#}$ does not matter: we always arrive at the same distribution at the point (t, s) along the trajectory prescribed by γ . This is formalized via

$$(\Phi_{\gamma(l)})\# \circ (\Psi_{0,\gamma^{(2)}(l)})\# p_{0,0} = (\Psi_{\gamma(l)})\# \circ (\Phi_{\gamma^{(1)}(l),0})\# p_{0,0}.$$

To preserve distributional path-independence, it is sufficient if there exists a single probability density path that satisfies continuity equations (3), that is, when $p_{t,s}$ and $q_{t,s}$ coincide for all t and s in $[0, 1]$. We formally state this as a lemma.

Lemma 3.1 (Path-independent transport of distributions). *Consider $u_{t,s}$ and $v_{t,s}$ vector fields. If there exists a unique generated probability density path $p_{t,s}$ satisfying (3), then the associated flows $\Phi_{t,s}$ and $\Psi_{t,s}$ satisfy (4).*

Lemma 3.1 provides a sufficient condition for path-independent transport of distributions. However, other sufficient conditions for this property exist. One way this can occur is when the system defined by (2) admits a unique joint trajectory $\phi_{t,s}$. This implies pointwise path independence, while for our formulation we only need distributional path independence, which is a weaker property. A necessary and sufficient condition for a unique solution $\phi_{t,s}$ to exist is provided in Proposition 19.29 of (Lee, 2003) which uses the partial differential equation described in (5).

Proposition 3.2 ((Pointwise) path-independence equation). *Suppose that the vector fields $u_{t,s}$ and $v_{t,s}$ are satisfy*

$$\partial_s u_{t,s} - \partial_t v_{t,s} = [u_{t,s}, v_{t,s}], \quad \forall x \in \mathbb{R}^d \quad (5)$$

where $\partial_s u_{t,s} := \partial u_{t,s}(x)/\partial s$, $\partial_t v_{t,s} := \partial v_{t,s}(x)/\partial t$, and $[\cdot, \cdot]$ is the Lie Bracket, $[u_{t,s}, v_{t,s}] := (\nabla_x u_{t,s}(x)) v_{t,s}(x) - (\nabla_x v_{t,s}(x)) u_{t,s}(x)$. Then there exists a unique flow $\Phi_{t,s}$ which satisfies (4).

3.2 Consistent and Path-independent Transport of Distributions in PiFM

We consider data distributions $q(a)$, $q(b)$ and $q(c)$, and the joint density $q(z)$ with $z = (a, b, c)$. In contrast to the traditional flow matching framework, we consider the probability density path $p : [0, 1]^2 \times \mathbb{R}^d \rightarrow \mathbb{R}_{\geq 0}$ of two-parameter with boundary conditions $p_{0,0}(x) = q(a)$, $p_{1,0}(x) = q(b)$ and $p_{0,1}(x) = q(c)$. Analogous to CFM, we condition on z yielding,

$$p_{t,s}(x) = \int p_{t,s}(x|z)q(z)dz, \quad (6)$$

where the conditional density path $p_{t,s}(x|z)$ is induced by some conditional vector fields $u_{t,s}(x|z)$ and $v_{t,s}(x|z)$. We seek two vector fields $u_{t,s}, v_{t,s} : [0, 1]^2 \times \mathbb{R}^d \rightarrow \mathbb{R}^d$ that generate $p_{t,s}$ by satisfying the continuity equations for all $t, s \in [0, 1]$

$$\frac{\partial p_{t,s}(x)}{\partial t} + \nabla \cdot (p_{t,s}(x) u_{t,s}(x)) = 0, \quad \frac{\partial p_{t,s}(x)}{\partial s} + \nabla \cdot (p_{t,s}(x) v_{t,s}(x)) = 0. \quad (7)$$

If the two equations above hold, then the corresponding flows satisfy the distributional path-independence property. Given conditional vector fields $u_{t,s}(x|z)$ and $v_{t,s}(x|z)$, we model the unconditional vector fields by

$$u_{t,s}(x) = \mathbb{E}_{q(z)} \left[\frac{u_{t,s}(x|z)p_{t,s}(x|z)}{p_{t,s}(x)} \right], \quad v_{t,s}(x) = \mathbb{E}_{q(z)} \left[\frac{v_{t,s}(x|z)p_{t,s}(x|z)}{p_{t,s}(x)} \right]. \quad (8)$$

We note that the precise forms of the conditional vector fields $u_{t,s}(x|z)$ and $v_{t,s}(x|z)$ are not prescribed a priori and left as a user-defined choice.

Theorem 3.3. *Let the conditional vector fields $u_{t,s}(x|z)$ and $v_{t,s}(x|z)$ generate the unique conditional probability density path $p_{t,s}(x|z)$ satisfying the analogous equations (7). Then, the vector fields $u_{t,s}(x)$ and $v_{t,s}(x)$ in (8) generate the unique probability density path $p_{t,s}(x)$ satisfying (7).*

Theorem 3.3 can be viewed as a generalization of the conditional-to-marginal generation result in CFM, extending the framework to accommodate multiple parameter settings and additional target distributions. As a corollary to Theorem 3.3 and Lemma 3.1, we have the following result: the flows of the unconditional vector fields have the distributional path-independence property.

Corollary 3.4 (Path-independent transport of distributions in PiFM). *Suppose that the vector fields $u_{t,s}(x|z)$ and $v_{t,s}(x|z)$ generate the unique conditional probability density path $p_{t,s}(x|z)$ satisfying the analogous equations (7). Then, the associated flows $\Phi_{t,s}$ and $\Psi_{t,s}$ of the vector fields $u_{t,s}(x)$ and $v_{t,s}(x)$ given in (8) satisfy (4).*

3.3 Training via Path-independent Flow Matching

Now we discuss a neural approach for training a PiFM model. Given two parameterized vector fields $u_{t,s}^\theta$ and $v_{t,s}^\theta$, PiFM learns the dynamics by regressing these fields onto the corresponding conditional vector fields. We define the flow-matching regression loss as

$$\mathcal{L}_{\text{FM}}(\theta) = \mathbb{E} \left[\|u_{t,s}^\theta(x) - u_{t,s}(x|z)\|^2 + \|v_{t,s}^\theta(x) - v_{t,s}(x|z)\|^2 \right]$$

For conditional vector fields that do not automatically satisfy the pointwise path-independence condition in (5), we consider additionally penalizing violations of this condition, this is particularly useful in settings such as integrating PiFM with Curly Flow Matching (Petrović et al., 2025); see Section 4.1.2. The path-independence regularizer is

$$\mathcal{L}_{\text{Pi}}(\theta) = \mathbb{E} \left[\left\| \partial_s u_{t,s}^\theta(x|z) - \partial_t v_{t,s}^\theta(x|z) - [u_{t,s}^\theta(x|z), v_{t,s}^\theta(x|z)] \right\|^2 \right].$$

Given a regularization weight $\lambda \geq 0$, the PiFM objective is $\mathcal{L}_{\text{PiFM}}(\theta; \lambda) = \mathcal{L}_{\text{FM}}(\theta) + \lambda \mathcal{L}_{\text{Pi}}(\theta)$. Training proceeds analogously to CFM. We sample $(t, s) \sim \mathcal{U}([0, 1]^2)$ and $z = (a, b, c) \sim q(z)$, where $q(z)$ may be specified using either independent coupling or an optimal-transport coupling. We then sample $x \sim p_{t,s}(\cdot | z)$ and update θ by minimizing $\mathcal{L}_{\text{PiFM}}(\theta; \lambda)$. The full training procedure is summarized in Algorithm 1.

One specific choice of conditional vector fields and conditional probability path is given by

$$u_{t,s}(x|z) = b - a, \quad v_{t,s}(x|z) = c - a, \quad p_{t,s}(x|z) = \mathcal{N}(x | \mu_{t,s}(z), \sigma^2), \quad (9)$$

for fixed $\sigma > 0$. This generalizes the affine interpolation commonly used in CFM to a multi-parameter setting by introducing a two-dimensional interpolation of the form $\mu_{t,s}(z) = a + (b-a)t + (c-a)s$. This choice of conditional vector fields and conditional probability density paths is guaranteed to induce unconditional vector fields that transport the marginal probability density path $p_{t,s}$ in a consistent and path-independent manner by satisfying both Theorem 3.3 and Corollary 3.4. Consequently, in this setting, enforcing commutativity via \mathcal{L}_{Pi} is not required. More general conditional vector fields and probability paths may also be used as long as consistency and path-independent transport of distributions is satisfied.

3.4 Relation to Wasserstein Barycenter

In the previous subsections, we discussed PiFM, its properties, and its training. Now, we show that PiFM empirically approximates the Wasserstein Barycenter between three distributions. Additionally, under suitable conditions, we provide theoretical guarantees that PiFM matches the Wasserstein barycenter, demonstrating that PiFM recovers a geometrically meaningful notion that is globally consistent with interpolation between distributions.

Let $\lambda := (\lambda_1, \dots, \lambda_K)$ with $\lambda_j \geq 0$ and $\sum_{j=1}^K \lambda_j = 1$ for some $K \in \mathbb{N}$. The Wasserstein barycenter ρ_λ of probability measures $\rho_1, \dots, \rho_K \in \mathcal{P}_2(\mathbb{R}^d)$ with finite second moment is a distribution that minimizes the multi-marginal optimal transport cost $J(\gamma, \lambda)$ given below

$$J(\gamma, \lambda) = \int \sum_{j=1}^K \lambda_j \|T_\lambda(x_1, \dots, x_K) - x_j\|^2 d\gamma,$$

over all couplings γ of ρ_1, \dots, ρ_K with $T_\lambda(x_1, \dots, x_K) = \sum_{j=1}^K \lambda_j x_j$.

One popular algorithm for computing the Wasserstein barycenter is the free support computation algorithm (Cuturi & Doucet, 2014), available in the POT package (Flamary et al., 2021). Empirically, we observe in Figure 2a. that distributions $\hat{\rho}_{t,s}^{\text{PiFM}}$ computed from our method coincide with the Wasserstein barycenter $WB_{1-t-s,t,s}(\rho_0, \rho_1, \rho_2)$ obtained with the free support algorithm. In addition, we visually observe that our framework extrapolates beyond the simplex constraint on λ in Figure 2b.

To support our claim that PiFM can approximate the Wasserstein barycenter, we provide additional experimental results in Supplementary Figure 7 on more complex distributions. In addition, using the multi-marginal optimal transport formulation and the notion of admissible families of deformations from (Boissard et al., 2013), Theorem 3.5 gives sufficient conditions under which the PiFM-generated distribution $\hat{\rho}_{t,s}$ is the minimizer of the Wasserstein barycenter objective. From the discussion in section 3.2 note that $\hat{\rho}_{t,s} = (\Phi_{t,s})_\# \circ (\Psi_{0,s})_\# \rho_0 = (\Psi_{t,s})_\# \circ (\Phi_{t,0})_\# \rho_0 =: \Gamma_{t,s}(\rho_0)$.

Theorem 3.5. Consider $\rho_0, \rho_1, \rho_2 \in \mathcal{P}(\mathbb{R}^d)$ with $\lambda = (1-t-s, t, s)$. Suppose that the optimal transport maps $T_1 : \rho_0 \rightarrow \rho_1$, $T_2 : \rho_0 \rightarrow \rho_2$ belong to an admissible family of deformations, and the conditional paths satisfy $z_{t,s}(a) = (1-t-s)a + tT_1(a) + sT_2(a)$. Then, under $\sigma \rightarrow 0$, PiFM approximates the Wasserstein barycenter between (ρ_0, ρ_1, ρ_2) , i.e., $\hat{\rho}_{t,s} = \Gamma_{t,s}(\rho_0)$ satisfies

Algorithm 1 Path-Independent Flow Matching (PiFM)

- 1: **Input:** Efficiently samplable $q(a, b, c)$, $p_{t,s}(x|(a, b, c))$, computable conditional vector fields $u_{t,s}(x|(a, b, c))$ and $v_{t,s}(x|(a, b, c))$, initial two-headed network (u^θ, v^θ) with a single backbone, learning rate $\eta > 0$ and regularization $\lambda > 0$.
- 2: **while** training **do**
- 3: Sample $(a, b, c) \sim q(a, b, c)$, $(t, s) \sim \mathcal{U}([0, 1]^2)$, $x \sim p_{t,s}(x|(a, b, c))$
- 4: Compute loss $\mathcal{L}_{\text{PiFM}}(\theta; \lambda)$
- 5: Update $\theta \leftarrow \theta - \eta \nabla_\theta \mathcal{L}_{\text{PiFM}}(\theta)$
- 6: **end while**
- 7: **return** u_θ, v_θ

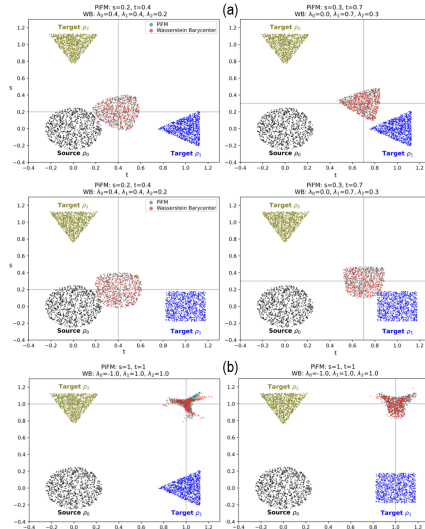


Figure 2: Comparison between output distributions from PiFM model (ours) and Wasserstein Barycenters for a) within and b) outside the probability simplex. The predicted distributions from the PiFM model correspond to the Wasserstein barycenters.

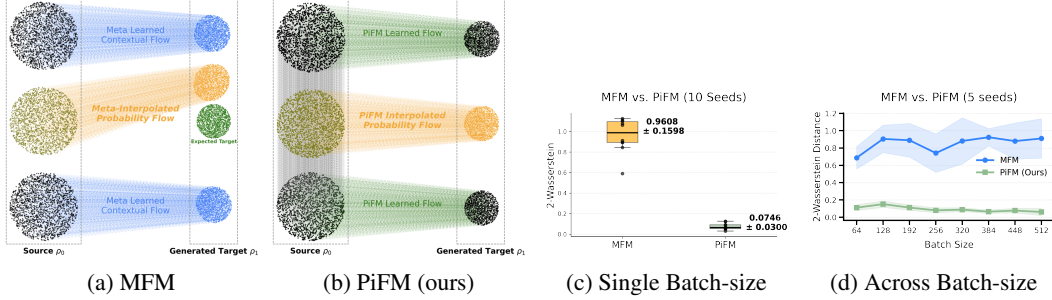


Figure 3: Comparison of Meta Flow Matching (MFM) and PiFM on a toy dataset, including qualitative trajectories and quantitative evaluation. Panels (a) and (b) show that MFM generalizes poorly to unseen source embeddings, while PiFM maintains consistent trajectories. Panels (c) and (d) report the 2-Wasserstein distance between ground truth and generated samples, showing that PiFM achieves more accurate and consistent transport.

$\hat{\rho}_{t,s} = WB_{\lambda}(\rho_0, \rho_1, \rho_2)$. Additionally, the optimal transport cost is

$$\int \left[(1-t-s) \|z_{t,s}(a) - a\|^2 + t \|z_{t,s}(a) - T_1(a)\|^2 + s \|z_{t,s}(a) - T_2(a)\|^2 \right] d\rho_0(a).$$

Additional results relating PiFM to the Wasserstein barycenter are presented in Appendix A.3 and Appendix B. Since computing the Wasserstein barycenter is computationally expensive, the results in this section highlight the potential of PiFM as a neural network-based alternative for approximating Wasserstein barycenters. Section B.1 provides an initial exploration of the computational time differences, while a more in-depth analysis is left for future work.

4 Experiments

We present empirical results for low- and high-dimensional data settings. In the low-dimensional setting, we demonstrate that PiFM outperforms Meta Flow Matching (MFM) in (Atanackovic et al., 2025) on a toy dataset under domain shift and show how PiFM can be incorporated with Curly Flow Matching Petrović et al. (2025). In the high-dimensional case, we evaluate PiFM’s performance on unsupervised image translation and demonstrate its superiority over traditional CFM in data extrapolation. We also evaluate on a real-world single-cell RNA-seq reprogramming dataset (Schiebinger et al., 2019), where PiFM models cellular states while jointly predicting experimental day and pluripotency score, testing whether the learned dynamics capture both chronological progression and fate acquisition toward successful reprogramming.

4.1 Low Dimensional Setting

To assess PiFM’s ability to infer samples under out-of-distribution conditions, we use synthetic data in which the distribution is shifted spatially in one direction and changes shape and shifts simultaneously in another direction.

4.1.1 PiFM for Inferring Unseen Population on Shifted Domain

Toy dataset. We construct unit discs with centers at $(0, 0)$ and $(0, 5)$ as training source distributions and small discs ($r = 0.5$) with centers at $(0, 5)$ and $(5, 5)$ as training target distributions. Given the unit disc with center at $(0, 2.5)$ as the unseen distribution in the source, the goal is to infer the small disc with center at $(5, 2.5)$ as expected target.

Comparison. Figure 3a shows that MFM has the correct flow (in blue) and target samples in the training set (top and bottom row), but misses the target on the test set (middle row). On the contrary, Figure 3b shows that PiFM predicts the correct flow and target from the unseen source distribution (middle row) by inferring the source distributions as samples on a “base” flow over the vertical direction. Moreover, we systematically evaluate the 2-Wasserstein distance between the predicted and expected target distributions over multiple runs of varying seeds. For the same number of batches ($= 512$) and training epochs ($= 3000$) for both MFM and PiFM over 10 random seeds, Figure 3c shows that the mean and standard deviation of 2-Wasserstein distance are much smaller for PiFM than for MFM, indicating the PiFM is more robust and accurate in this task. For same number of training epochs ($= 2000$) with varying batch sizes, PiFM consistently shows better performance (Figure 3d).

4.1.2 PiFM for Inferring Desirable Path-independent Distributions

Toy dataset. We evaluate PiFM in the Curly Flow Matching setting (Petrović et al., 2025), where the goal is to compose a rotation flow ($x_0 \rightarrow -x_0$) and an expansion flow ($x_0 \rightarrow 3x_0$) to produce a joint

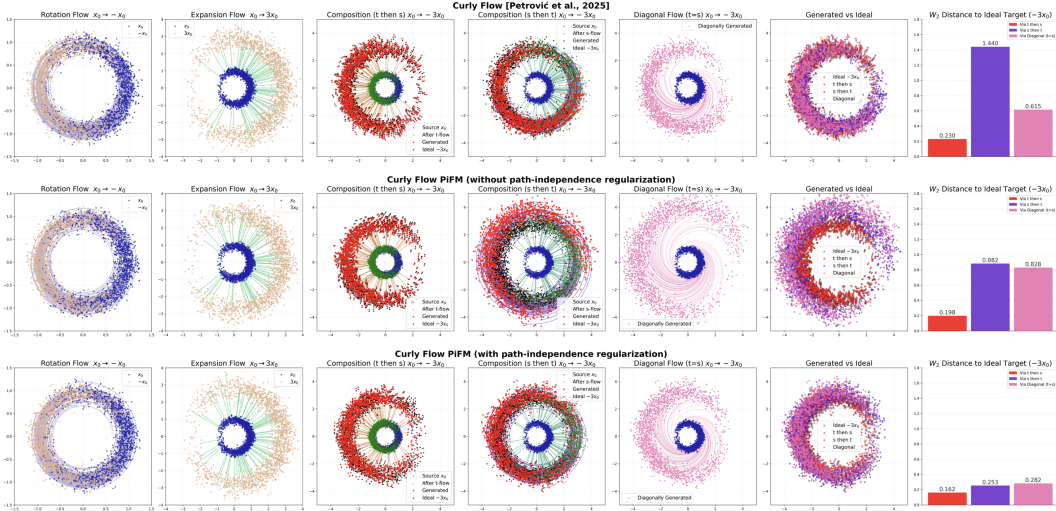


Figure 4: Illustration of PiFM in the Curly Flow Matching setting (Petrović et al., 2025) together with a quantitative evaluation of path dependence. Curly-FM and unregularized PiFM produce path-dependent dynamics and inconsistent final distributions across integration strategies. In contrast, PiFM with path-independence regularization yields consistent transport and the lowest value in Wasserstein-2 distance to the target distribution.

transformation $x_0 \rightarrow -3x_0$. A path-independent model should yield the same target distribution regardless of the integration strategy used at inference time.

Comparison. As shown in Figure 4, the original Curly-FM model, which trains the two vector fields separately, fails to achieve commutativity: sequential and diagonal integration paths produce inconsistent results, revealing path-dependent dynamics. PiFM without regularization also fails to recover commutativity despite joint training. In contrast, PiFM with path-independence regularization produces consistent outputs across all paths, with generated distributions closely matching the target distribution. This is further confirmed quantitatively in Figure 4, where Curly-FM and unregularized PiFM exhibit large variations in Wasserstein-2 distance across integration strategies. PiFM with path-independence regularization achieves the lowest values, demonstrating that enforcing commutativity during training is key to reliable path-independent generation.

4.2 High-Dimensional Setting: PiFM for Unsupervised Image-to-Image Translation

We train and evaluate on the CelebA (Liu et al., 2015) dataset using the Smiling and Black_Hair attributes. We employ a shared U-Net backbone with two per-pixel MLP heads implemented as 1×1 convolutions with SiLU activations, each predicting the vector field associated with one attribute flow. A full description of the preprocessing and architecture is provided in Appendix B.

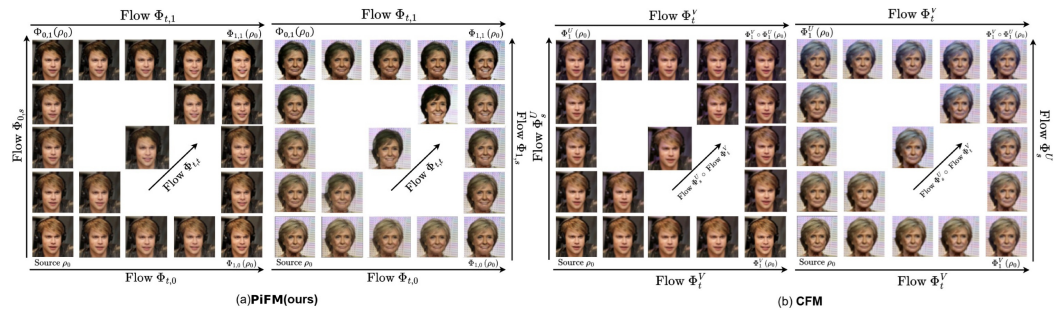


Figure 5: We present an image-to-image translation comparison of PiFM on the CelebA (Liu et al., 2015) dataset under three different flow integration strategies. PiFM successfully infers the missing attribute, whereas CFM fails to produce the desired transformation.

Figure 5 shows qualitative results for female (panel (a) right and (b) right) and male (panel (a) left and (b) left) examples across the three different flow integration strategies: $t \rightarrow s$, $s \rightarrow t$ and diagonal. In the PiFM results, the A-field (Smiling) produces localized mouth/cheek edits consistent with smiling, while the B-field (Black_Hair) darkens and re-textures the hair region. Note that the identity (global face shape, eyes) is largely preserved. The diagonal integration often produces

smoother simultaneous edits to both attributes. In contrast, CFM often fails to modify the source image along either one or both flow axes (e.g., CFM cannot generate smiling faces in Figure 5). Additional comparisons using FID are presented in Appendix B.2.3. We find FID poorly suited for evaluating commutativity as in Figure 5, since baseline methods may generate images close in pixel space without achieving the desired attribute transformations.

4.3 High-Dimensional Multi-Step Setting: PiFM for Single-Cell Reprogramming

We further evaluate PiFM on a real-world single-cell RNA-seq reprogramming dataset (Schiebinger et al., 2019). Data source and preprocessing details are provided in Appendix B.3.1. Cells are represented in 50-dimension PCA space, and the two biological axes are experimental day and pluripotency score. This setting provides a high-dimensional, multi-step biological test case: experimental day captures chronological reprogramming, while pluripotency score reflects acquisition of the target iPSC-like fate. Thus, the task evaluates whether PiFM can jointly model temporal dynamics and fate acquisition, rather than treating reprogramming as a single ordered trajectory.

As shown in Figure 6, PiFM-inferred trajectories evolve coherently along both biological axes, capturing temporal reprogramming at fixed pluripotency and fate acquisition at fixed experimental day. Moreover, when transporting day 0 low-pluripotency cells to day 6 high-pluripotency targets, different integration orders yield overlapping trajectories and generated distributions that align with the real target population, supporting path-independent generation. Biologically, this suggests that PiFM can model reprogramming as a multi-step and heterogeneous process, where cells observed at the same experimental day may occupy different intermediate states and only a subset progresses toward the pluripotent iPSC-like fate. We evaluate target prediction quality and commutativity in Appendix B.3.2.

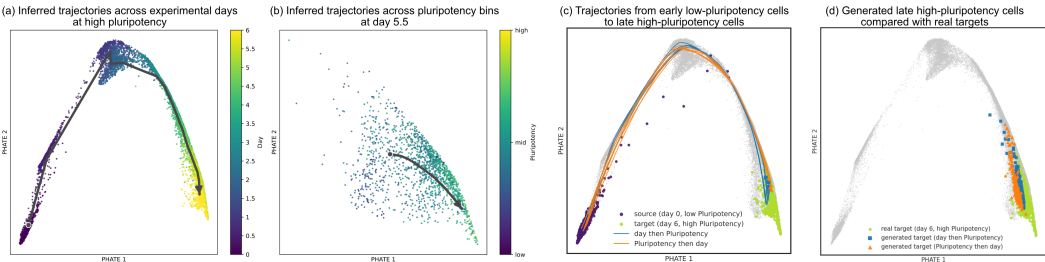


Figure 6: PiFM-inferred single-cell reprogramming dynamics across experimental day and pluripotency progression, visualized by PHATE Moon et al. (2019). (a) and (b) show trajectories along each biological axis, varying experimental day at fixed high pluripotency and varying pluripotency bins at fixed experimental day. (c) and (d) show path-ordered generation from day 0 low-pluripotency cells to day 6 high-pluripotency targets, where the two integration orders produce overlapping trajectories and generated distributions that match the real target population.

5 Discussion

Conclusion We introduced Path-Independent Flow Matching (PiFM), a multi-parameter Flow Matching that enforces consistent path-independent transport of distributions. We also make a connection between PiFM and Wasserstein barycenters. We showed that empirically, PiFM outperforms existing approaches on synthetic and image translation tasks, particularly in order-invariant and out-of-distribution settings. We further demonstrated applications to Curly Flow Matching and single-cell RNA-seq trajectory inference.

Limitations While our theory provides conditions for path-independent transport at the distribution level, it does not guarantee path independence for individual samples. Moreover, the connection to the Wasserstein barycenter is only studied in the $n = 2$ setting; further investigation is needed to establish the result in this work for the more general case.

Future Work Promising future directions include extending PiFM to more general geometries, as in Chen & Lipman (2024), and further applying it to single-cell perturbation data and trajectory inference tasks. Additionally, we will focus on validating PiFM as a Wasserstein barycenter generative framework beyond the setting discussed here.

6 Acknowledgements

This research was partially funded by FRQNT–NSERC grant 2023-NOVA-329125, the Courtois Institute, NSERC Discovery grants, and CIHR Program grants. The content provided here is solely the responsibility of the authors and does not necessarily represent the official views of the funding agencies.

References

- Agueh, M. and Carlier, G. Barycenters in the wasserstein space. *SIAM Journal on Mathematical Analysis*, 43(2):904–924, 2011.
- Albergo, M. S. and et al. Multimarginal generative modeling with stochastic interpolants. *arXiv preprint arXiv:2310.03695*, 2023.
- Albergo, M. S. and Vanden-Eijnden, E. Building normalizing flows with stochastic interpolants, 2023. URL <https://arxiv.org/abs/2209.15571>.
- Atanackovic, L., Zhang, X., Amos, B., Blanchette, M., Lee, L. J., Bengio, Y., Tong, A., and Neklyudov, K. Meta flow matching: Integrating vector fields on the wasserstein manifold, 2025. URL <https://arxiv.org/abs/2408.14608>.
- Beier, F., von Lindheim, J., Neumayer, S., and Steidl, G. Unbalanced multi-marginal optimal transport. *Journal of Mathematical Imaging and Vision*, 65(3):394–413, October 2022. ISSN 1573-7683. doi: 10.1007/s10851-022-01126-7. URL <http://dx.doi.org/10.1007/s10851-022-01126-7>.
- Berner, J., Richter, L., and Ullrich, K. An optimal control perspective on diffusion-based generative modeling. In *NeurIPS 2022 Workshop on Score-Based Methods*, 2022. URL https://openreview.net/forum?id=jlgs_E-0UdM.
- Bigot, J. and Klein, T. Characterization of barycenters in the wasserstein space by averaging optimal transport maps, 2017. URL <https://arxiv.org/abs/1212.2562>.
- Boissard, E., Gouic, T. L., and Loubes, J.-M. Distribution’s template estimate with wasserstein metrics, 2013. URL <https://arxiv.org/abs/1111.5927>.
- Bortoli, V. D., Thornton, J., Heng, J., and Doucet, A. Diffusion schrödinger bridge with applications to score-based generative modeling, 2023. URL <https://arxiv.org/abs/2106.01357>.
- Cao, J., Mo, L., Zhang, Y., Jia, K., Shen, C., and Tan, M. Multi-marginal wasserstein gan. In *Advances in Neural Information Processing Systems*, volume 32, 2019.
- Chen, R. T. and Lipman, Y. Flow matching on general geometries. In *12th International Conference on Learning Representations, ICLR 2024 ; Conference date: 07-05-2024 Through 11-05-2024*, January 2024.
- Chen, R. T. Q., Rubanova, Y., Bettencourt, J., and Duvenaud, D. Neural ordinary differential equations, 2019. URL <https://arxiv.org/abs/1806.07366>.
- Cuturi, M. Sinkhorn distances: Lightspeed computation of optimal transport. In *Advances in Neural Information Processing Systems (NeurIPS)*, pp. 2292–2300, 2013.
- Cuturi, M. and Doucet, A. Fast computation of wasserstein barycenters. In *Proceedings of Machine Learning Research*, volume 32, pp. 685–693. Journal of Machine Learning Research, 2014.
- Diederik, P. K. and Max, W. An introduction to variational autoencoders. *Foundations and Trends® in Machine Learning*, 12(4):307–392, November 2019. ISSN 1935-8245. doi: 10.1561/22000000056. URL <http://dx.doi.org/10.1561/22000000056>.
- Fatras, K., Sejourne, T., Flamary, R., and Courty, N. Unbalanced minibatch optimal transport; applications to domain adaptation. In Meila, M. and Zhang, T. (eds.), *Proceedings of the 38th International Conference on Machine Learning*, volume 139 of *Proceedings of Machine Learning Research*, pp. 3186–3197. PMLR, 18–24 Jul 2021. URL <https://proceedings.mlr.press/v139/fatras21a.html>.

- Flamary, R., Courty, N., Gramfort, A., Alaya, M. Z., Boisbunon, A., Chambon, S., Chapel, L., Corenflos, A., Fatras, K., Fournier, N., et al. Pot: Python optimal transport. *Journal of Machine Learning Research*, 22(78):1–8, 2021. URL <http://jmlr.org/papers/v22/20-451.html>.
- Goodfellow, I. J., Pouget-Abadie, J., Mirza, M., Xu, B., Warde-Farley, D., Ozair, S., Courville, A., and Bengio, Y. Generative adversarial networks, 2014. URL <https://arxiv.org/abs/1406.2661>.
- Grathwohl, W., Chen, R. T. Q., Bettencourt, J., Sutskever, I., and Duvenaud, D. Ffjord: Free-form continuous dynamics for scalable reversible generative models, 2018. URL <https://arxiv.org/abs/1810.01367>.
- Ho, J., Jain, A., and Abbeel, P. Denoising diffusion probabilistic models, 2020. URL <https://arxiv.org/abs/2006.11239>.
- Jiang, L., Dalgarno, C., Papalexi, E., Mascio, I., Wessels, H.-H., Yun, H., Iremadze, N., Lithwick-Yanai, G., Lipson, D., and Satija, R. Systematic reconstruction of molecular pathway signatures using scalable single-cell perturbation screens. *Nature Cell Biology*, 27:505–517, 02 2025. doi: 10.1038/s41556-025-01622-z.
- Kingma, D. P. and Welling, M. Auto-encoding variational bayes, 2022. URL <https://arxiv.org/abs/1312.6114>.
- Koehler, F., Heckett, A., and Risteski, A. Statistical efficiency of score matching: The view from isoperimetry, 2022. URL <https://arxiv.org/abs/2210.00726>.
- Lee, J. M. Introduction to smooth manifolds. In *Introduction to smooth manifolds*, pp. 1–29. Springer, 2003.
- Lipman, Y., Chen, R. T. Q., Ben-Hamu, H., Nickel, M., and Le, M. Flow matching for generative modeling, 2023. URL <https://arxiv.org/abs/2210.02747>.
- Liu, G.-H., Vahdat, A., Huang, D.-A., Theodorou, E. A., Nie, W., and Anandkumar, A. I²sb: Image-to-image schrödinger bridge, 2023. URL <https://arxiv.org/abs/2302.05872>.
- Liu, Q. Rectified flow: A marginal preserving approach to optimal transport, 2022. URL <https://arxiv.org/abs/2209.14577>.
- Liu, Z., Luo, P., Wang, X., and Tang, X. Deep learning face attributes in the wild. In *Proceedings of the IEEE international conference on computer vision*, pp. 3730–3738, 2015.
- Lotfollahi, M., Klimovskaia Susmelj, A., De Donno, C., Hetzel, L., Ji, Y., Ibarra, I. L., Srivatsan, S. R., Naghypourfar, M., Daza, R. M., Martin, B., et al. Predicting cellular responses to complex perturbations in high-throughput screens. *Molecular Systems Biology*, pp. e11517, 2023.
- Léonard, C. A survey of the schrödinger problem and some of its connections with optimal transport, 2013. URL <https://arxiv.org/abs/1308.0215>.
- Moon, K. R., Van Dijk, D., Wang, Z., Gigante, S., Burkhardt, D. B., Chen, W. S., Yim, K., Elzen, A. v. d., Hirn, M. J., Coifman, R. R., et al. Visualizing structure and transitions in high-dimensional biological data. *Nature biotechnology*, 37(12):1482–1492, 2019.
- Neary, C. and Topcu, U. Compositional learning of dynamical system models using port-hamiltonian neural networks, 2023. URL <https://arxiv.org/abs/2212.00893>.
- Pass, B. Multi-marginal optimal transport: Theory and applications. *ESAIM: Mathematical Modelling and Numerical Analysis*, 49(6):1771–1790, 2015. doi: 10.1051/m2an/2015020. URL <https://www.numdam.org/articles/10.1051/m2an/2015020/>.
- Petrović, K., Atanackovic, L., Moro, V., Kapuśniak, K., İsmail İlkan Ceylan, Bronstein, M., Bose, A. J., and Tong, A. Curly flow matching for learning non-gradient field dynamics, 2025. URL <https://arxiv.org/abs/2510.26645>.
- Ralph Abraham, J. E. M. and Ratiu, T. Manifolds, tensor analysis, and applications. *SIAM Review*, 26(4):590–592, 1984. doi: 10.1137/1026118.

- S, K. and Durgadevi, M. Generative adversarial network (gan): a general review on different variants of gan and applications. In *2021 6th International Conference on Communication and Electronics Systems (ICCES)*, pp. 1–8, 2021. doi: 10.1109/ICCES51350.2021.9489160.
- Schiebinger, G., Shu, J., Tabaka, M., Cleary, B., Subramanian, V., Solomon, A., Gould, J., Liu, S., Lin, S., Berube, P., Lee, L., Chen, J., Brumbaugh, J., Rigollet, P., Hochedlinger, K., Jaenisch, R., Regev, A., and Lander, E. S. Optimal-transport analysis of single-cell gene expression identifies developmental trajectories in reprogramming. *Cell*, 176(4):928–943.e22, 2019. doi: 10.1016/j.cell.2019.01.006.
- Song, Y., Sohl-Dickstein, J., Kingma, D. P., Kumar, A., Ermon, S., and Poole, B. Score-based generative modeling through stochastic differential equations, 2021. URL <https://arxiv.org/abs/2011.13456>.
- Tong, A., Malkin, N., Huguët, G., Zhang, Y., Rector-Brooks, J., Fatras, K., Wolf, G., and Bengio, Y. Improving and generalizing flow-based generative models with minibatch optimal transport, 2023.
- Tong, A., Malkin, N., Fatras, K., Atanackovic, L., Zhang, Y., Huguët, G., Wolf, G., and Bengio, Y. Simulation-free schrödinger bridges via score and flow matching, 2024. URL <https://arxiv.org/abs/2307.03672>.
- Wang, Y., Li, Z., Zhang, Z., Zhang, W., Xie, B., Liu, X., Zeng, W., and Jin, X. Scene graph disentanglement and composition for generalizable complex image generation, 2024. URL <https://arxiv.org/abs/2410.00447>.
- Warner, F. *Foundations of Differentiable Manifolds and Lie Groups*. Graduate Texts in Mathematics. Springer, 1983. ISBN 9780387908946. URL <https://books.google.ca/books?id=iaeUqc2yQVQC>.
- Wiggins, S. *Introduction to Applied Nonlinear Dynamical Systems and Chaos*, volume 2 of *Texts in Applied Mathematics*. Springer, New York, 2003. ISBN 978-0-387-00177-7.

A Theoretical Details and Proofs

A.1 The general multi-parameter case

PiFM generalizes to the case of multiple parameters t_1, \dots, t_n . In this setting, we consider a source data distribution $q(a)$ and target data distributions $q(b_1), \dots, q(b_n)$. We condition on the joint distribution $q(z)$, where $z = (a, b_1, \dots, b_n)$, with a marginalization,

$$p_{t_1, \dots, t_n}(x) = \int p_{t_1, \dots, t_n}(x | z) q(z) dz. \quad (10)$$

The continuously differentiable vector fields $u_{t_1, \dots, t_n}^{(i)}$ are associated with the ODEs

$$\frac{\partial \phi^{(i)}(x)_{t_1, \dots, t_n}}{\partial t_i} = u_{t_1, \dots, t_n}^{(i)}(\phi_{t_1, \dots, t_n}(x)) \quad (11)$$

Each vector field $u_{t_1, \dots, t_n}^{(i)}$ governs the evolution from the source distribution $q(a)$ to the target distribution $q(b_i)$ and has an associated flow $\Phi_{t_1, \dots, t_n} : [0, 1]^n \times \mathbb{R}^d \rightarrow \mathbb{R}^d$, $\Phi_{t_1, \dots, t_n}(x) = \phi_{t_1, \dots, t_n}(x)$. We define

$$u_{t_1, \dots, t_n}^{(i)}(x) = \mathbb{E}_{q(z)} \left[\frac{u_{t_1, \dots, t_n}^{(i)}(x|z) p_{t_1, \dots, t_n}(x|z)}{p_{t_1, \dots, t_n}(x)} \right] \quad (12)$$

for all $i = 1, \dots, n$.

Here, $u_{t_1, \dots, t_n}^{(i)}(x|z)$ are the conditional vector fields. We consider the n continuity equations

$$\frac{\partial p_{t_1, \dots, t_n}(x)}{\partial t_i} + \nabla \cdot (p_{t_1, \dots, t_n}(x) u_{t_1, \dots, t_n}^{(i)}(x)) = 0, \quad (13)$$

which hold for all $t_j \in [0, 1]$ with $j \neq i$. Additionally, the path-independence property (4) is replaced by a family of equalities corresponding to integrating along each parameter direction sequentially, resulting in $n!$ equivalent expressions. Finally, (5) is replaced by $\binom{n}{2}$ conditions encoding pairwise consistency between vector fields. For all $i, j = 1, \dots, n$, $i \neq j$, we obtain

$$\partial_{t_i} u_{t_1, \dots, t_n}^{(i)}(x) - \partial_{t_j} u_{t_1, \dots, t_n}^{(j)}(x) = [u_{t_1, \dots, t_n}^{(i)}(x), u_{t_1, \dots, t_n}^{(j)}(x)] \quad (14)$$

The generalized version of the affine probability path and conditional vector fields is as follows. We take

$$u_{t_1, \dots, t_n}^{(i)}(x|z) = b_i - a, \quad \forall i = 1, \dots, n$$

and

$$p_{t_1, \dots, t_n}(x|z) = \mathcal{N}(x | \mu_{t_1, \dots, t_n}(z), \sigma^2)$$

with constant $\sigma > 0$ and $\mu_{t_1, \dots, t_n}(z) = a + \sum_{i=1}^n (b_i - a) t_i$. As discussed in the main part of the paper, the choice of conditional vector fields and probability paths is a user defined choice as long as there is consistent and path-independent distribution transport.

A.2 Proofs of theorems

Lemma A.1 (General form Lemma 3.1). *Consider $u_{t_1, \dots, t_n}^{(i)}(x)$ vector fields. If there exists a unique generated probability density path $p_{t_1, \dots, t_n}(x)$ satisfying (13), then the associated flows $\Phi_{t_1, \dots, t_n}^{(i)}(x)$ satisfy the path-independence condition.*

Proof. Suppose that the vector fields $u_T^{(i)}(x)$ generate $p_T(x)$,

$$\frac{\partial p_T(x)}{\partial t_i} + \nabla \cdot (p_T(x) u_T^{(i)}(x)) = 0, \quad \forall i = 1, \dots, n.$$

There are $n!$ possible orderings in which one can successively transport along each coordinate, starting from $(0, \dots, 0)$ and reaching $T = (t_1, \dots, t_n)$. Without loss of generality, it suffices to consider the ordering $t_1 \rightarrow t_2 \rightarrow \dots \rightarrow t_n$, as all other cases follow analogously.

We proceed iteratively. First, we transport using the flow $\Phi_{t_1,0,\dots,0}^{(1)}$ which is associated to the vector field $u_T^{(1)}$, obtaining $(\Phi_{t_1,0,\dots,0}^{(1)})_{\#} p_{0,\dots,0}$. Next, we transport using $\Phi_{t_1,t_2,0,\dots,0}^{(2)}$, yielding $(\Phi_{t_1,t_2,0,\dots,0}^{(2)})_{\#} \circ (\Phi_{t_1,0,\dots,0}^{(1)})_{\#} p_{0,\dots,0}$. Continuing in this manner, we arrive at the expression

$$(\Phi_{t_1,\dots,t_n}^{(n)})_{\#} \circ \dots \circ (\Phi_{t_1,t_2,0,\dots,0}^{(2)})_{\#} \circ (\Phi_{t_1,0,\dots,0}^{(1)})_{\#} p_{0,\dots,0}.$$

Since the vector fields $u_T^{(i)}$ jointly generate $p_T(x)$, it follows that at $T = (t_1, \dots, t_n)$ we have

$$(\Phi_{t_1,\dots,t_n}^{(n)})_{\#} \circ \dots \circ (\Phi_{t_1,t_2,0,\dots,0}^{(2)})_{\#} \circ (\Phi_{t_1,0,\dots,0}^{(1)})_{\#} p_{0,\dots,0} = p_{t_1,\dots,t_n}.$$

Repeating the same argument for the remaining $n! - 1$ orderings, and noting that each construction yields p_{t_1,\dots,t_n} , we conclude that all $n!$ resulting expressions coincide. \square

Proposition A.2 (General form of Proposition 3.2). *Suppose that the vector fields $u_{t_1,\dots,t_n}^{(i)}(x)$ satisfy the integrability condition (14) Then there exists a unique flow Φ_{t_1,\dots,t_n} which satisfies the path-independence property.*

Proof. Suppose that the vector fields $u_T^{(i)}$ satisfy the integrability condition

$$\partial_{t_i} u_{t_1,\dots,t_n}^{(i)} - \partial_{t_j} u_{t_1,\dots,t_n}^{(j)} = [u_{t_1,\dots,t_n}^{(i)}, u_{t_1,\dots,t_n}^{(j)}]$$

By Proposition 19.29 in (Lee, 2003), there exists a unique solution ϕ_{t_1,\dots,t_n} to the system

$$\frac{\partial \phi_{t_1,\dots,t_n}(x)}{\partial t_i} = u_{t_1,\dots,t_n}^{(i)}(\phi_{t_1,\dots,t_n}(x)), \quad \forall i = 1, \dots, n,$$

In this case, the map $\Phi : [0, 1]^n \times \mathbb{R}^d \rightarrow \mathbb{R}^d$, defined by

$$\Phi_{t_1,\dots,t_n}(x) = \phi_{t_1,\dots,t_n}(x),$$

is the unique flow associated with the family of vector fields $u_T^{(i)}$. It follows that transporting along the flows $\Phi^{(i)}$, which in this case is Φ , in any order yields the same result. \square

Theorem A.3 (General form of Theorem 3.3). *Let the conditional vector fields $u_{t_1,\dots,t_n}^{(i)}(x|z)$ generate the unique conditional probability density path $p_{t_1,\dots,t_n}(x|z)$ satisfying the analogous equations (13). Then, the vector fields $u_{t_1,\dots,t_n}^{(i)}(x)$ in (12) generate the unique probability density path $p_{t_1,\dots,t_n}(x)$ satisfying (13).*

Proof. Suppose that the conditional vector fields $u_{t_1,\dots,t_n}^{(i)}(x|z)$ generate $p_{t_1,\dots,t_n}(x|z)$. That is,

$$\frac{\partial p_{t_1,\dots,t_n}(x|z)}{\partial t_i} + \nabla \cdot (p_{t_1,\dots,t_n}(x|z) u_{t_1,\dots,t_n}^{(i)}(x|z)) = 0, \quad \forall i = 1, \dots, n.$$

Then,

$$\begin{aligned} -\nabla \cdot (p_{t_1,\dots,t_n}(x) u_{t_1,\dots,t_n}^{(i)}(x)) &= -\nabla \cdot \left(p_{t_1,\dots,t_n}(x) \int u_{t_1,\dots,t_n}^{(i)}(x|z) \frac{p_{t_1,\dots,t_n}(x|z) q(z)}{p_{t_1,\dots,t_n}(x)} dz \right) \\ &= -\nabla \cdot \left(\int u_{t_1,\dots,t_n}^{(i)}(x|z) p_{t_1,\dots,t_n}(x|z) q(z) dz \right) \\ &= -\int \nabla \cdot (u_{t_1,\dots,t_n}^{(i)}(x|z) p_{t_1,\dots,t_n}(x|z) q(z)) dz \\ &= -\int \nabla \cdot (u_{t_1,\dots,t_n}^{(i)}(x|z) p_{t_1,\dots,t_n}(x|z)) q(z) dz \\ &= \int \frac{\partial p_{t_1,\dots,t_n}(x|z)}{\partial t_i} q(z) dz \\ &= \frac{\partial}{\partial t_i} \int p_{t_1,\dots,t_n}(x|z) q(z) dz \\ &= \frac{\partial p_{t_1,\dots,t_n}(x)}{\partial t_i}. \end{aligned}$$

Therefore, the vector fields $u_{t_1,\dots,t_n}^{(i)}$ generate $p_{t_1,\dots,t_n}(x)$. \square

Corollary A.4 (General form of Corollary 3.4). *Suppose that the vector fields $u_{t_1, \dots, t_n}(x|z)$ generate the unique conditional probability density path $p_{t_1, \dots, t_n}(x|z)$ satisfying the analogous equations (13). Then, the associated flows $\Phi_{t_1, \dots, t_n}^{(i)}$ of the vector fields $u_{t_1, \dots, t_n}^{(i)}(x)$ given in (12) satisfy the path-independence property.*

Proof. Suppose that the conditional vector fields $u_{t_1, \dots, t_n}^{(i)}(x|z)$ generate $p_{t_1, \dots, t_n}(x|z)$. By Theorem 3.3, it follows that the vector fields $u_{t_1, \dots, t_n}^{(i)}(x)$ generate $p_{t_1, \dots, t_n}(x)$. Finally, by Lemma 3.1, transporting along the flows $\Phi_{t_1, \dots, t_n}^{(i)}$ in any order yields the same result. \square

A.3 Discussion about the relation between PiFM and Wasserstein Barycenter

We hereafter discuss Theorem 3.5 and the connection between PiFM and Wasserstein Barycenter.

Lemma A.5 (Lemma 3.1 of Boissard et al. (2013)). *Let $\Pi(\mu_1, \dots, \mu_K)$ be the set of probability measures on $(\mathbb{R}^d)^K$ with marginals μ_1, \dots, μ_K , respectively, and*

$$T(x_1, \dots, x_K) = \sum_{1 \leq j \leq K} \lambda_j x_j$$

with $\lambda_j \geq 0$ such that $\sum_{1 \leq j \leq K} \lambda_j = 1$. A probability measure ν is a barycenter of μ_1, \dots, μ_K with weights $(\lambda_j)_{1 \leq j \leq K}$ if and only if $\nu = T\#\gamma$ where $\gamma \in \Pi(\mu_1, \dots, \mu_K)$ minimizes the multi marginal Optimal Transport:

$$J(\gamma, \lambda) = \int \sum_{j=1}^K \lambda_j \|T(x_1, \dots, x_K) - x_j\|^2 d\gamma(x_1, \dots, x_K) \quad (15)$$

By choosing T as $T(a, b, c) = a + t(b - a) + s(c - a) = (1 - t - s)a + tb + sc$ and $\lambda = (1 - t - s, t, s)$ we have:

$$J(\gamma, \lambda) = \int \left[(1 - t - s) \|T(a, b, c) - a\|^2 + t \|T(a, b, c) - b\|^2 + s \|T(a, b, c) - c\|^2 \right] d\rho_0(a) \rho_1(b) \rho_2(c)$$

With Optimal Coupling such that $b = T_1(a)$ and $c = T_2(a)$, T only depends on a and we have $T(a, b, c) = z_{t,s}(a)$ and the associated multi marginal transport is defined as

$$J^{\text{PiFM}}(\rho_0, \lambda) := \int \left[(1 - t - s) \|z_{t,s}(a) - a\|^2 + t \|z_{t,s}(a) - T_1(a)\|^2 + s \|z_{t,s}(a) - T_2(a)\|^2 \right] d\rho_0(a) \quad (16)$$

Without specific assumptions, $J^{\text{PiFM}}(\rho_0, \lambda)$ is not guaranteed to be a minimizer of (15). In the following, we give sufficient conditions referred to as the admissible family of deformations under which $J^{\text{PiFM}}(\rho_0, \lambda)$ minimizes (15).

Theorem A.6 (Theorem 4.1 of Boissard et al. (2013)). *Suppose that $(T_i)_{1 \leq i \leq K}$ is an admissible family of deformations on a domain $\Omega \subset \mathbb{R}^n$, and let $\mu \in \mathcal{P}_2(\Omega)$ be absolutely continuous with respect to the Lebesgue measure. Let $\mu_j = (T_j)\#\mu$, $\mu = (\mu_j)_{1 \leq j \leq K}$ and $\lambda = (\lambda_j)_{1 \leq j \leq K}$. Then,*

$$WB(\mu, \lambda) = \left(\sum_{j=1}^K \lambda_j T_j \right) \# \mu \quad (17)$$

The notion of an admissible family of deformations is defined in Boissard et al. (2013) (Definition 4.2) as follows:

1. there exists j_0 such that $T_{j_0} = \text{Id}$
2. for each $1 \leq j \leq K$: T_j is one-to-one and onto,
3. the composition $T_i \circ T_j^{-1}$ of two maps in this class remains an optimal one for all $1 \leq i, j \leq K$

We now prove Theorem 3.5.

Proof of Theorem 3.5. Let's first recall that with optimal coupling such that $b = T_1(a)$ and $c = T_2(a)$ and in the limit of $\sigma \rightarrow 0$, we have $T(a, b, c) = z_{t,s}(a) = a + (1-t)T_1(a) + (1-s)T_2(b)$. Therefore, by construction:

$$\hat{\rho}_{t,s} := \Gamma_{t,s}(\rho_0) \quad (18)$$

$$:= ((1-t-s)\text{Id} + tT_1 + sT_2)_{\#}\rho_0 \quad (19)$$

where we recall that $\Gamma_{t,s}(\rho_0) = (\Phi_{t,s})_{\#} \circ (\Psi_{0,s})_{\#}\rho_0 = (\Psi_{t,s})_{\#} \circ (\Phi_{t,0})_{\#}\rho_0$. Equation (19) can be rewritten as

$$\hat{\rho}_{t,s} = \left(\sum_{j=1}^K \lambda_j T_j \right)_{\#} \rho_0$$

Assuming that T_1 and T_2 belong to the admissible family of deformation, using Theorem A.6 we get that $\hat{\rho}_{t,s}$ is exactly the Wasserstein Barycenter, i.e PiFM generates the Wasserstein barycenter of ρ_0, ρ_1, ρ_2 with $\lambda = (1-t-s, t, s)$, this concludes the proof.

Additionally, using (16) and applying Lemma A.5, we get:

$$\begin{aligned} J^{\text{PiFM}}(\rho_0, \lambda) &= \int \left[(1-t-s) \|z_{t,s}(a) - a\|^2 + t \|z_{t,s}(a) - T_1(a)\|^2 + s \|z_{t,s}(a) - T_2(a)\|^2 \right] d\rho_0(a) \\ &= \underset{\gamma}{\text{argmin}} J(\gamma, \lambda) \end{aligned}$$

□

A.4 Additional results relating PiFM to the Wasserstein Barycenter

We note that not only the model predicts the Wasserstein barycenter within the simplex defined by ρ_0, ρ_1 and ρ_2 , but we also empirically observe that for toy distributions outside of this simplex, $\rho_{t,s}^{\text{PiFM}}$ coincides with the horizontal barycenter $\rho_s^U(t)$ (resp. vertical barycenter $\rho_t^V(s)$) after applying $\Gamma_{0,s}$ (resp. $\Gamma_{t,0}$) to the initial and target distributions as shown in Supplementary Figure 12 and in Supplementary Figure 13. Below, we discuss the Gaussian case with proof related to horizontal and vertical Wasserstein barycenter.

Theorem A.7. *Let $m_0, m_1, m_2 \in \mathbb{R}^d$. Suppose that there exists a symmetric positive semidefinite matrix $\Sigma \in \mathbb{R}^{d \times d}$ such that*

$$\rho(0) = \mathcal{N}(m_0, \Sigma), \quad \rho(1) = \mathcal{N}(m_1, \Sigma), \quad \rho(2) = \mathcal{N}(m_2, \Sigma).$$

Define the conditional vector fields

$$\hat{u}_{t,s}(x) := u_{t,s}(x|z) := m_1 - m_0, \quad \hat{v}_{t,s}(x) := v_{t,s}(x|z) := m_2 - m_0,$$

and, for $(t, s) \in \Delta^2 := \{(t, s) \in [0, 1]^2 : t + s \leq 1\}$, define

$$\hat{Q}_{t,s} := \mathcal{N}\left((1-t-s)m_0 + tm_1 + sm_2, \Sigma\right).$$

Let $\mathcal{Q}_{t,s}$ denote the probability measure with density $\hat{Q}_{t,s}$.

Then:

(i) The family $\hat{Q}_{t,s}$ satisfies the two continuity equations

$$\partial_t \hat{Q}_{t,s} + \nabla \cdot (\hat{Q}_{t,s} \hat{u}) = 0, \quad \partial_s \hat{Q}_{t,s} + \nabla \cdot (\hat{Q}_{t,s} \hat{v}) = 0,$$

with boundary conditions

$$\hat{Q}_{0,0} = \rho(0), \quad \hat{Q}_{1,0} = \rho(1), \quad \hat{Q}_{0,1} = \rho(2).$$

(ii) For every $(t, s) \in \Delta^2$, $\mathcal{Q}_{t,s}$ is the Wasserstein barycenter of $\rho(0), \rho(1), \rho(2)$ with weights $(1-t-s, t, s)$, i.e.,

$$\mathcal{Q}_{t,s} = \underset{\nu \in \mathcal{P}_2(\mathbb{R}^d)}{\text{argmin}} \left\{ (1-t-s) \mathcal{W}_2^2(\nu, \rho(0)) + t \mathcal{W}_2^2(\nu, \rho(1)) + s \mathcal{W}_2^2(\nu, \rho(2)) \right\}.$$

(iii) The horizontal and vertical slice barycenter identities also hold:

(a) For each fixed $s \in [0, 1]$, define

$$A_s := (\Psi_s^0)_\# \rho(0), \quad B_s := (\Psi_s^1)_\# \rho(1).$$

Then

$$A_s = \mathcal{N}(m_0 + s(m_2 - m_0), \Sigma), \quad B_s = \mathcal{N}(m_1 + s(m_2 - m_0), \Sigma),$$

and for every $t \in [0, 1]$,

$$\mathcal{Q}_{t,s} = \arg \min_{\nu \in \mathcal{P}_2(\mathbb{R}^d)} \left\{ (1-t) \mathcal{W}_2^2(\nu, A_s) + t \mathcal{W}_2^2(\nu, B_s) \right\}.$$

(b) For each fixed $t \in [0, 1]$, define

$$C_t := (\Phi_t^0)_\# \rho(0), \quad D_t := (\Phi_t^1)_\# \rho(2).$$

Then

$$C_t = \mathcal{N}(m_0 + t(m_1 - m_0), \Sigma), \quad D_t = \mathcal{N}(m_2 + t(m_1 - m_0), \Sigma),$$

and for every $s \in [0, 1]$,

$$\mathcal{Q}_{t,s} = \arg \min_{\nu \in \mathcal{P}_2(\mathbb{R}^d)} \left\{ (1-s) \mathcal{W}_2^2(\nu, C_t) + s \mathcal{W}_2^2(\nu, D_t) \right\}.$$

Proof of Theorem A.7. Set

$$\gamma := \mathcal{N}(0, \Sigma), \quad \tau_m(x) := x + m.$$

Then

$$\rho(i) = (\tau_{m_i})_\# \gamma, \quad i = 0, 1, 2.$$

Step 1: Explicit form of the flow and continuity equations.

Since \hat{u} and \hat{v} are constant vector fields, their flows are translations:

$$\Phi_{t,s}(x) = x + t(m_1 - m_0), \quad \Psi_{t,s}(x) = x + s(m_2 - m_0).$$

Hence

$$(\Phi_{t,s})_\# \rho(0) = \mathcal{N}(m_0 + t(m_1 - m_0), \Sigma),$$

and

$$(\Psi_{t,s})_\# \rho(0) = \mathcal{N}(m_0 + s(m_2 - m_0), \Sigma).$$

Hence,

$$\mathcal{Q}_{t,s} = \mathcal{N}(m_0 + t(m_1 - m_0) + s(m_2 - m_0), \Sigma) = \hat{Q}_{t,s}.$$

Since $\hat{Q}_{t,s}$ is a translated Gaussian with constant covariance and its mean evolves according to the constant velocities \hat{u}, \hat{v} , it satisfies

$$\partial_t \hat{Q}_{t,s} + \nabla \cdot (\hat{Q}_{t,s} \hat{u}) = 0, \quad \partial_s \hat{Q}_{t,s} + \nabla \cdot (\hat{Q}_{t,s} \hat{v}) = 0.$$

The boundary conditions are immediate from the definition.

Step 2: Global barycenter identity.

Let

$$\lambda_0 := 1 - t - s, \quad \lambda_1 := t, \quad \lambda_2 := s, \quad (\lambda_0, \lambda_1, \lambda_2) \in \Delta^2.$$

Set

$$\bar{m}_{t,s} := \lambda_0 m_0 + \lambda_1 m_1 + \lambda_2 m_2.$$

Then

$$\mathcal{Q}_{t,s} = \mathcal{N}(\bar{m}_{t,s}, \Sigma) = (\tau_{\bar{m}_{t,s}})_\# \gamma.$$

We claim that $\mathcal{Q}_{t,s}$ minimizes

$$J(\nu, \lambda) := \sum_{i=0}^2 \lambda_i \mathcal{W}_2^2(\nu, \rho(i)).$$

Take any $\nu \in \mathcal{P}_2(\mathbb{R}^d)$, and let m_ν denote its mean. Write $\tilde{\nu} := (\tau_{-m_\nu})\#\nu$, so that $\tilde{\nu}$ has mean zero.

For each i , since $\rho(i) = (\tau_{m_i})\#\gamma$, any coupling of ν and $\rho(i)$ may be written in terms of random variables $Y \sim \nu$, $X \sim \gamma$. Expanding the square gives (because the cross term vanishes):

$$\mathbb{E}|Y - (X + m_i)|^2 = \mathbb{E}|(Y - m_\nu) - X|^2 + |m_\nu - m_i|^2,$$

Taking the infimum over couplings yields

$$\mathcal{W}_2^2(\nu, \rho(i)) \geq \mathcal{W}_2^2(\tilde{\nu}, \gamma) + |m_\nu - m_i|^2.$$

Therefore

$$J(\nu, \lambda) \geq \mathcal{W}_2^2(\tilde{\nu}, \gamma) + \sum_{i=0}^2 \lambda_i |m_\nu - m_i|^2.$$

Since $\sum_i \lambda_i = 1$, the quadratic function

$$m \mapsto \sum_{i=0}^2 \lambda_i |m - m_i|^2$$

is uniquely minimized at

$$m = \sum_{i=0}^2 \lambda_i m_i = \bar{m}_{t,s}.$$

Also,

$$\mathcal{W}_2^2(\tilde{\nu}, \gamma) \geq 0,$$

with equality if and only if $\tilde{\nu} = \gamma$, i.e.

$$\nu = (\tau_{\bar{m}_{t,s}})\#\gamma = \mathcal{Q}_{t,s}.$$

Thus $\mathcal{Q}_{t,s}$ is the unique minimizer of F .

This step could also be simply demonstrated using Theorem 3.5 as Φ_t^s and Ψ_s^t belong to an admissible family of deformation.

Step 3: Horizontal slice barycenter identity.

Fix $s \in [0, 1]$. Since $\Psi_{t,s}$ is translation by $s(m_2 - m_0)$,

$$A_s = (\Psi_{0,s})\#\rho(0) = \mathcal{N}(m_0 + s(m_2 - m_0), \Sigma),$$

and

$$B_s = (\Psi_{1,s})\#\rho(1) = \mathcal{N}(m_1 + s(m_2 - m_0), \Sigma).$$

Their weighted $(1-t, t)$ -barycenter is therefore the Gaussian with the same covariance Σ and mean

$$(1-t)(m_0 + s(m_2 - m_0)) + t(m_1 + s(m_2 - m_0)) = m_0 + t(m_1 - m_0) + s(m_2 - m_0),$$

which is exactly the mean of $\mathcal{Q}_{t,s}$. Hence $\mathcal{Q}_{t,s}$ is the horizontal barycenter.

Step 4: Vertical slice barycenter identity.

Fix $t \in [0, 1]$. Since $\Phi_{t,s}$ is translation by $t(m_1 - m_0)$,

$$C_t = (\Phi_{t,0})\#\rho(0) = \mathcal{N}(m_0 + t(m_1 - m_0), \Sigma),$$

and

$$D_t = (\Phi_{t,0})\#\rho(2) = \mathcal{N}(m_2 + t(m_1 - m_0), \Sigma).$$

Their weighted $(1-s, s)$ -barycenter is the Gaussian with covariance Σ and mean

$$(1-s)(m_0 + t(m_1 - m_0)) + s(m_2 + t(m_1 - m_0)) = m_0 + t(m_1 - m_0) + s(m_2 - m_0),$$

again equal to the mean of $\mathcal{Q}_{t,s}$. Thus $\mathcal{Q}_{t,s}$ is also the vertical barycenter. This proves the theorem. \square

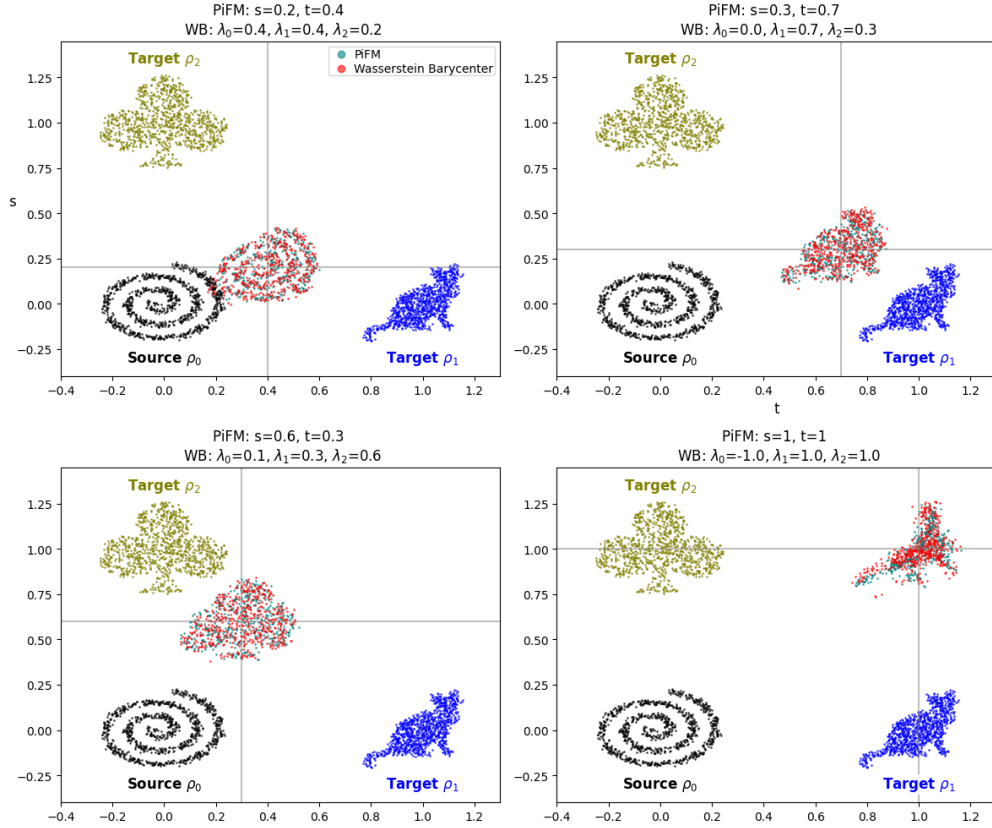


Figure 7: Comparison between output distributions from PiFM model (ours) and Wasserstein Barycenters for a) within and b) outside the probability simplex for spiral, clover and cat distributions . The predicted distributions from the PiFM model correspond to the Wasserstein Barycenters.

B Additional Experimental Details and Results

B.1 Comparison of execution times for PiFM and Free Support Algorithm (PyOT)

it is worth noting that computing Wasserstein barycenters is very expensive, even with the fast free-support computation implementation in the POT package. We compare execution time between the former and show that our method considerably reduces the time required to compute the barycenter (Supplementary Figure 8) and state that PiFM can be leveraged for fast inference of Wasserstein barycenters, with most of the computational cost incurred during model training.

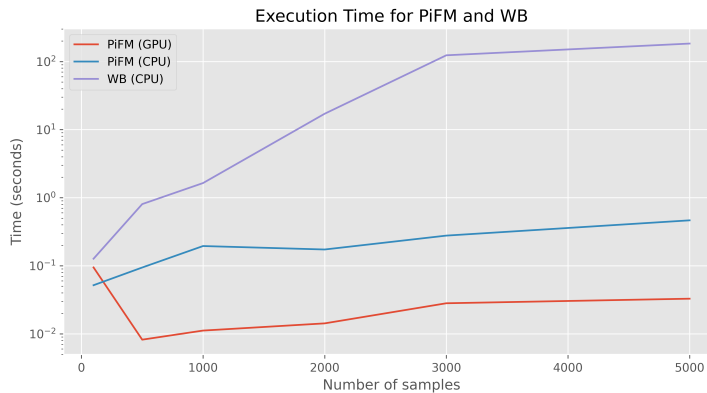


Figure 8: Comparison of execution times between free support barycenter (POT package) and PiFM (ours).

B.2 Supplementary Details and Results for Unsupervised Image-to-Image Translation

B.2.1 Dataset, Preprocessing and Model architecture for Image-to-Image Translation

We train and evaluate on the CelebA dataset (Liu et al., 2015). From the official split we extract images and attribute labels, and use two attributes in the joint experiment: *Smiling* (attribute A) and *Black_Hair* (attribute B). Each image is center-cropped to 178, resized to 64×64 , converted to a tensor and normalized to $[-1, 1]$ (per-channel mean 0.5, std 0.5). For training we partition the dataset into four subsets by attribute presence: *sources* (neither A nor B), *A-only* (has A, not B), *B-only* (has B, not A), and *both*.

For model architecture, We use a shared UNet backbone with two per-pixel MLP heads implemented as 1×1 convolutions (equivalent to applying a small MLP independently at every spatial location) with *SiLU* non-linear activation function. Each of these two MLPs outputs the vector field corresponding to the flow or progression along each of the attributes mentioned above. Details of the model architecture used in this experiment are summarized in Table 1 in Appendix B.

Table 1: Summary of the model architecture used in the unsupervised image-to-image translation experiment (Section 4.2).

Subnetwork	Component	# PWE	Input / Output	Details
UNet backbone	Encoder (downpath): [128 \rightarrow 256 \rightarrow 256 \rightarrow 256], 2 Res-Blocks per level	2*	3 / 128	Downsampling encoder with residual blocks per stage
	Bottleneck (mid): 256 channels with attention	2*	128 / 128	Residual blocks + attention at mid-resolution
	Decoder (uppath): [256 \rightarrow 256 \rightarrow 128 \rightarrow 128]	2*	128 / 128	Symmetric upsampling with skip connections
Per-pixel MLP (Head_h)	Conv MLP: 128 \rightarrow 128 \rightarrow 3 (Conv1x1 + SiLU + Conv1x1)	2	128 / 3	Predicts per-pixel field $v(t, x)$
Per-pixel MLP (Head_v)	Conv MLP: 128 \rightarrow 128 \rightarrow 3 (Conv1x1 + SiLU + Conv1x1)	2	128 / 3	Predicts per-pixel field $v(t, x)$
Prediction semantics	-	-	(B,3,H,W)	Output is per-pixel displacement field $v(t, x)$

* “# PWE” indicates number of residual blocks per level.

B.2.2 Meta Flow Matching (MFM) as a baseline for unsupervised image-to-image translation

The original meta flow matching (MFM) (Atanackovic et al., 2025) work was developed and evaluated on low-dimensional point-cloud tasks (letters, trellis) where each training environment is a compact 2D point distribution and the model architecture is a GNN + flow decoder tailored to that setting. To test whether the MFM method, the alternating meta-style optimization that jointly learns per-environment embeddings and a conditional flow decoder, can scale to high-dimensional image data, we adapted the MFM pipeline to the CelebA (Liu et al., 2015) image dataset. Our goal was to keep the MFM training dynamics intact while replacing dataset- and architecture-specific pieces so that the same meta-learning principle can operate on images and produce composed transformations (e.g., smiling + aging).

Point-cloud environments and images are different in data dimensionality, spatial structure, and inductive biases. GNNs operate on unordered point sets and they are a suitable for letters, but they are not appropriate for dense image signals. To respect image structure and give the flow decoder expressive local features and to have a fair comparison with what we proposed in our PiFM pipeline, we replaced the original encoder/decoder backbone with a the same image backbone we used in our PiFM pipeline (architecture details are presented in Table 1: a U-Net-style feature extractor paired with small per-task MLP heads. This preserves the essential MFM decomposition: an encoder that produces a per-environment representation and a decoder that predicts flow fields conditioned on that representation, while providing the right inductive bias for images. Moreover, similar to MFM, we used two-optimizer alternating training: a flow optimizer that updates the decoder MLP heads to match conditional flow targets and an encoder optimizer that updates the backbone embeddings (the meta parameters). Alternating these updates encourages the encoder to produce embeddings that

generalize across environments while the decoder learns to follow them. All other core MFM choices (the flow-matching objective, sampling of interpolation times, EMA for evaluation snapshots, and the alternating schedule itself) were left intact so that any differences in outcome can be attributed to the change in data domain and architecture rather than to changes in the meta-method. At training, a practical issue when moving to images is how to pair source images (neither attribute) with target images (A-only or B-only) for supervised flow targets. We used nearest-neighbor (OT-style pairing) on flattened image features (or simple L2 in pixel space for diagnostics) to create target displacements. At inference we generate composed A+B outputs by integrating the sum of the two learned vector fields (or by sequential integrations $t \rightarrow$ or $s \rightarrow$), which mirrors the composition strategy used in our PiFM experiments.

We kept the same evaluation philosophy: visualize sample trajectories (frames along integration paths) and compute distribution distances between predicted distributions and target distributions using the same metrics used for point-cloud experiments. In Figure 9, we provide grids of intermediate frames for the three integration strategies (t-then-s, s-then-t, diagonal/combined) so readers can see whether composition produces plausible joint-attribute images. As shown, MFM fails to modify the source image along either one or both flow axes.

Training and sampling. We train two conditional vector fields simultaneously: (i) $v_h(t, x)$, vector field for attribute A (Smiling), and (ii) $v_v(s, x)$, vector field for attribute B (Black_Hair). On each training step we sample a minibatch of source images $\{x_a\}$ (from *sources*), target-A images $\{x_b\}$ (from *A-only*) and target-B images $\{x_c\}$ (from *B-only*). Each source is paired to a semantically similar target in the corresponding target minibatch using mini-batch discrete optimal transport (EMD) on flattened pixel vectors; denote the aligned targets by x_b^{aligned} and x_c^{aligned} . We optimize the network with Adam (base learning rate of 2×10^{-4}), gradient clipping of 1.0 and a linear warm-up schedule. An exponential moving average (EMA, decay 0.999) of the model parameters is maintained and used for visualization similar to (Tong et al., 2023).

Inference. Let N_{steps} be the integer number of update steps chosen for the inference (we use Euler updates of step size $1/N_{\text{steps}}$). The three flow integration strategies implemented are: (i) *Integrate t then s* ($t \rightarrow s$): First integrate the A-field from $t = 0$ to 1, then integrate the B-field from $s = 0$ to 1. We split the total number of steps into two parts (approximately half for the first phase, half for the second) so the total frame count equals $N_{\text{steps}} + 1$. At each sub-step we update: $x \leftarrow x + \frac{1}{N_{\text{phase}}} v_h(t, x)$ or $x \leftarrow x + \frac{1}{N_{\text{phase}}} v_v(s, x)$, depending on the phase. (ii) *Integrate s then t* ($s \rightarrow t$): Same as above but apply the B-field first and the A-field second. Order-of-application is intentionally swapped to reveal commutativity. (iii) *Integrate diagonally* ($t = s$): Integrate along the diagonal $t = s = \tau$ from 0 to 1. At each step evaluate both fields and take their sum: $v(\tau, x) = v_h(\tau, x) + v_v(\tau, x)$, $x \leftarrow x + \frac{1}{N_{\text{steps}}} v(\tau, x)$. This approximates simultaneous application of both vector fields.



Figure 9: Image-to-image translation results of Meta Flow Matching (MFM) on CelebA (Liu et al., 2015) dataset across three different flow integration strategies. The A-field (Smiling) produces localized mouth/cheek edits consistent with smiling, while the B-field (Young) darkens and re-textures the hair region. As shown, MFM fails to modify the source image along either one or both flow axes.



Figure 10: More results on the Image-to-image translation task for PiFM on CelebA (Liu et al., 2015) dataset across three different flow integration strategies. The A-field (Smiling) produces localized mouth/cheek edits consistent with smiling, while the B-field (Black Hair) darkens and re-textures the hair region.

B.2.3 FID Evaluation of Commutativity

Standard image fidelity metrics such as FID are not well suited for evaluating PiFM on the commutativity task (Figure 5), as baseline methods often produce images that are close in pixel space without achieving the desired attribute changes. Figure 11 illustrates this limitation by applying FID to the experiment in Figure 5 in an attempt to quantify commutativity.

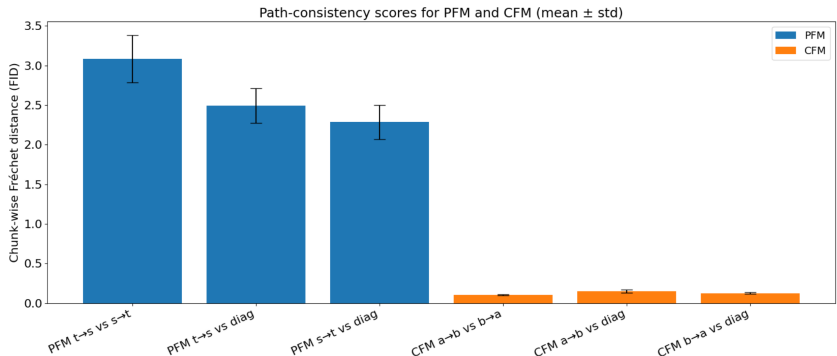


Figure 11: Quantitative experiment for commutativity of PiFM using FID, comparison with CFM. Based on the experiment in Section 4.2.

B.3 Single-Cell Experiment

B.3.1 Data Source and Preprocessing

We use the public MEF-to-iPSC reprogramming single-cell RNA-seq dataset (Schiebinger et al., 2019), using the serum-condition H5AD file from Figshare article 20051492. The raw object is already normalized and log-transformed. We keep cells from the serum condition, downsample to at most 1,500 cells per experimental day, and focus on the early reprogramming window from day 0 to day 6 at half-day resolution. This yields 19,492 cells after filtering.

For the state representation, we select up to 3,000 highly variable genes, scale expression values with maximum value 10, and compute a 50-dimensional PCA embedding. We use this PCA representation as the input space for PiFM; PHATE embeddings are computed only for visualization. The two biological axes are experimental day and the provided Pluripotency signature score. Experimental day represents chronological reprogramming, while the pluripotency score measures acquisition of an iPSC-like identity. For balanced grouping and diagnostics, we additionally split the pluripotency score within each day into low, middle, and high tertiles.

B.3.2 Evaluation of Prediction and Commutativity

We evaluate whether the two integrated composition orders produce consistent endpoint distributions, and whether these endpoints occupy the same region as the empirical target distribution. The source distribution is always the day 0, low-pluripotency group, and the comparison is performed over 39 endpoint groups, corresponding to 12 day intervals and 3 pluripotency-bin intervals. To make distances comparable across groups with different source-target scales, we report centroid distance and sliced Wasserstein distance normalized by the corresponding source-to-target distance.

As shown in Table 2, the two composition orders produce endpoint distributions that are close to each other relative to the overall source-target scale. Comparing each endpoint to the empirical target further shows that both compositions land in the same broad target regional, though they are not exactly identical. This imperfect agreement is expected because each endpoint is obtained by composing learned vector fields over relatively long day and pluripotency intervals, so small local integration and approximation errors can accumulate along the trajectory.

Table 2: Target distribution consistency measured by normalized centroid distance and normalized sliced Wasserstein distance. The metrics evaluate whether the two composition orders produce similar endpoint distributions and whether each endpoint lies in the same target region as the empirical distribution.

Comparison	Normalized centroid	Normalized W_2
day then Pluripotency vs true	0.6979 ± 0.1263	0.7917 ± 0.1684
Pluripotency then day vs true	0.5651 ± 0.1255	0.6601 ± 0.1691
day then Pluripotency vs Pluripotency then day	0.3459 ± 0.0572	0.3465 ± 0.0560

B.4 Comparison of distributions obtained from PiFM (ours) and Wasserstein barycenters using Free Support Algorithm (PyOT) for different values t, s

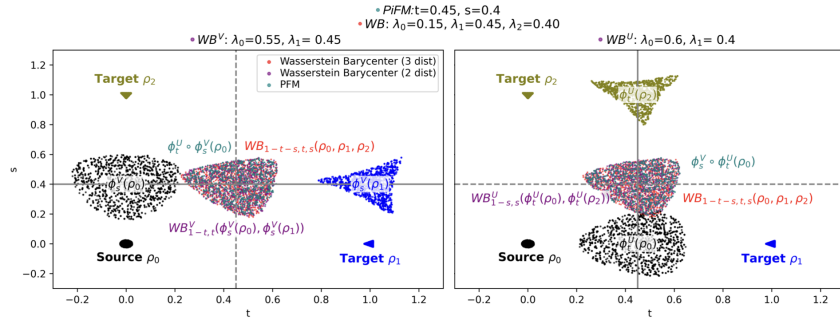


Figure 12: Comparison between output distributions from PiFM (ours), global Wasserstein barycenter and Wasserstein barycenters between ϕ_s^V (left) and ϕ_t^U (right) projections for $t=0.45, s=0.4$. Source and target distributions are rescaled for clarity.

B.5 Comparison of distributions obtained from PiFM (ours), Wasserstein barycenters using Free Support Algorithm (PyOT) between source and targets and vertical and horizontal Wasserstein barycenters

In the following, we define $\phi_{t,s=0}(\rho)$ as the output distribution from the push forward operation $(\phi_t^U)_\#$ of ρ with fixed $s = 0$, i.e the horizontal integration of the vector field for $t' \in [0, t]$ and $s = 0$. Similarly, we define $\phi_{t=1,s}(\rho)$ as the output distribution from the push forward operation $(\phi_s^V)_\#$ of ρ with fixed $t = 1$, i.e the integration of the vector field for $s' \in [0, s]$ and $t = 1$.

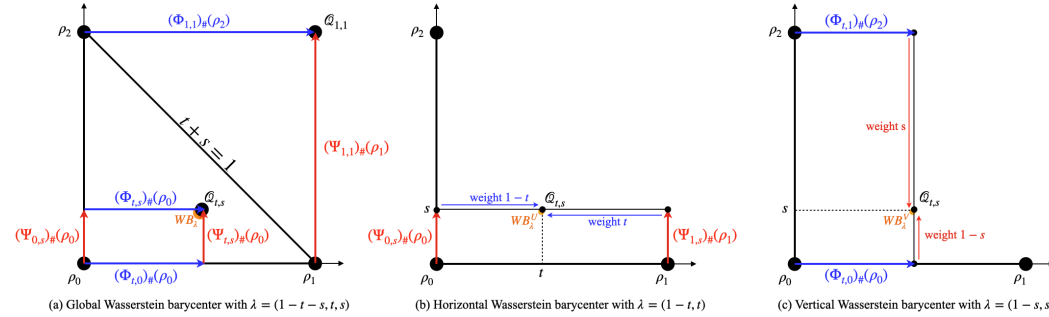


Figure 13: a) the global (t, s) -diagram with the simplex $\Delta = \{(t, s) \in [0, 1] : t + s \leq 1\}$ and commuting paths. b) the horizontal slice for fixed s . c) the vertical slice for fixed t .

Supplementary Figures 14 and 15 provide additional comparisons at different values of (t, s) , showing that the PiFM output agrees with the global Wasserstein barycenter and with the corresponding horizontal and vertical slice barycenters.

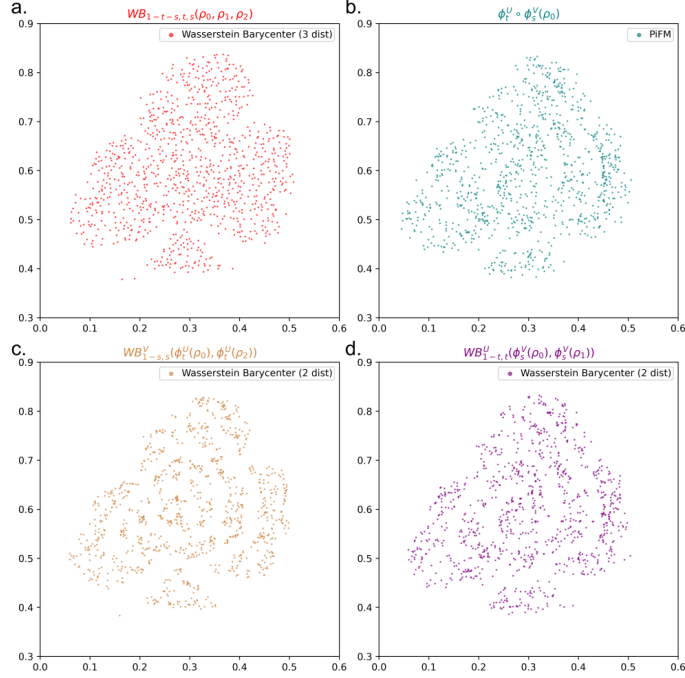


Figure 14: Comparison between output distributions from a) Wasserstein Barycenters with weights $(1 - t - s, t, s) = (0.1, 0.6, 0.3)$ (using Free Support Algorithm) b) PiFM model (ours) with $t = 0.6, s = 0.3$, c) vertical Wasserstein barycenter with $\lambda = (1 - t, t) = (0.4, 0.6)$ computed using Free Support Algorithm of $\phi_{t,s=0}(\rho_0)$ and $\phi_{t,s=1}(\rho_2)$ with $t = 0.6$, d) horizontal Wasserstein barycenter $\lambda = (1 - s, s) = (0.7, 0.3)$ computed using Free Support Algorithm of $\phi_{t=0,s}(\rho_0)$ and $\phi_{t=1,s}(\rho_1)$ with $s = 0.3$

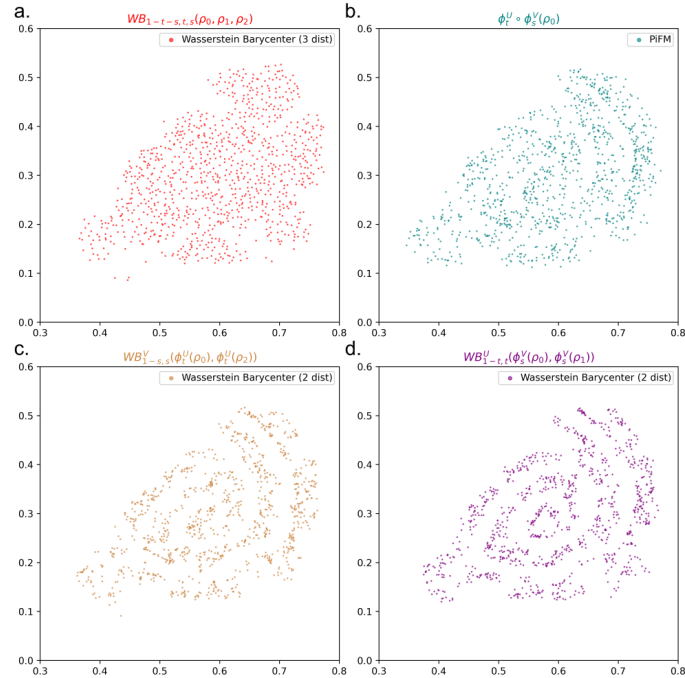


Figure 15: Comparison between output distributions from a) Wasserstein Barycenters with weights $(1 - t - s, t, s) = (0.1, 0.3, 0.6)$ (using Free Support Algorithm) b) PiFM model (ours) with $t = 0.3, s = 0.6$, c) vertical Wasserstein barycenter with $\lambda = (1 - t, t) = (0.7, 0.3)$ computed using Free Support Algorithm of $\phi_{t,s=0}(\rho_0)$ and $\phi_{t,s=1}(\rho_2)$ with $t = 0.3$, d) horizontal Wasserstein barycenter $\lambda = (1 - s, s) = (0.4, 0.6)$ computed using Free Support Algorithm of $\phi_{t=0,s}(\rho_0)$ and $\phi_{t=1,s}(\rho_1)$ with $s = 0.6$